BEILSTEIN JOURNAL OF ORGANIC CHEMISTRY

Supporting Information

for

Interfragment interactions in outer-sphere radical addition control *Z*-selectivity in iron-catalyzed allene dialkylation

Zihan Li, Yin-Hon Yeung and Xinglong Zhang

Beilstein J. Org. Chem. **2026,** *22,* 1761–1772. doi:10.3762/bjoc.22.142

Detailed computational methods, visualizations of the DFT-optimized structures, and absolute energies obtained from the Gaussian calculations

License and Terms: This is a supporting information file under the terms of the Creative Commons Attribution License (https://creativecommons.org/licenses/by/4.0). Please note that the reuse, redistribution and reproduction in particular requires that the author(s) and source are credited and that individual graphics may be subject to special legal provisions.
The license is subject to the *Beilstein Journal of Organic Chemistry* terms and conditions: (https://www.beilstein-journals.org/bjoc/terms)

Table of contents

I. Computational methods *S2*

II. Model reaction and DFT functional benchmarking *S4*

III. Formation and regeneration of species **I** *S6*

IV. Distortion/interaction analyses for **TS1**/**TS1'**, **TS3**/**TS3'**, and **TS4**/**TS4'** *S7*

V. Visualization for DFT-optimized structures *S8*

VI. Optimized structures and absolute energies *S19*

References *S22*

I. Computational methods

Kohn–Sham density functional theory (KS-DFT) calculations were performed with *Gaussian 16 rev. B.01*[1]. Geometry optimizations were performed using the B3LYP hybrid functional[2-5] with Grimme's D3 dispersion correction with Becke-Johnson damping[6] (hereafter denoted B3LYP-D3BJ) and the def2-SVP[7,8] Karlsruhe-family basis set for all atoms. Minima and transition structures on the potential energy surface (PES) were confirmed using harmonic frequency analysis at the same level of theory, showing respectively zero and one imaginary frequency. Where appropriate, intrinsic reaction coordinate (IRC)[9,10] analysis was carried out to connect the appropriate reactant/product states passing through a given transition state.

Single-point (SP) corrections were performed using B3LYP-D3BJ and def2-TZVP[7,8] basis set for all atoms. The SMD implicit continuum solvation model[11] was used to account for the effect of tetrahydrofuran (THF) solvent on the computed Gibbs energy profile. To further assess the suitability of the chosen level of theory, separate single-point energy calculations were also carried out for all chemical species using the global-hybrid meta-NGA (nonseparable gradient approximation) MN15 functional[12] with the def2-TZVP basis set in implicit THF solvation using the SMD model. This functional was selected because it has been reported to perform well in predicting transition-metal reaction barrier heights[12] and is capable of describing systems with possible multireference character, which may be relevant to iron-catalyzed radical pathways.

Gibbs free energies were evaluated at the reaction temperature of 333.15 K (60 °C), using natural abundance weighted mass and a quasi-RRHO treatment of vibrational entropies and enthalpies[13,14]. Vibrational entropies of frequencies below 100 cm^{-1} were corrected according to a free rotor description, using Grimme's smooth damping function to interpolate between the two limiting descriptions[13]. For vibrational enthalpy, the quasi-RRHO correction proposed by Head-Gordon was adopted by modifying the vibrational internal energy expression before deriving the enthalpy, a cutoff value of 100 cm^{-1} was used[14]. The corrections were implemented using the thermochemistry analysis codes in *CHEMSMART* software[15]. The free energies reported in Gaussian from gas-phase optimization were further corrected using standard concentration of 1.0 mol/L[16], which

were used in solvation calculations, instead of the gas-phase 1.0 atm used by default in the *Gaussian 16* program.

For species involving open-shell characteristics, including doublet, triplet, quartet, quintet and sextet radicals, we performed above-mentioned DFT methodologies using the unrestricted formalism of the Kohn–Sham theory (UKS-DFT). The eigenvalues of the spin operator S^2 after annihilation of spin contamination were checked to ensure that they comply with the expected value of $S(S+1) = 0.75$ for a doublet wavefunction and $S(S+1) = 2$ for triplet, $S(S+1) = 3.75$ for quartet, $S(S+1) = 6$ for quintet, $S(S+1) = 8.75$ for sextet, indicating that spin contamination is not a problem for the present methodology.

Unless otherwise stated, the final corrected SMD(THF)-B3LYP-D3BJ/def2-TZVP//B3LYP-D3BJ/def2-SVP and SMD(THF)-MN15/def2-TZVP//B3LYP-D3BJ/def2-SVP Gibbs energies are both reported, with the latter set of values given in parenthesis. For example, if the relative energy of a species is given as 11.2 (11.5) kcal/mol, then 11.2 kcal/mol is obtained from SMD(THF)-B3LYP-D3BJ/def2-TZVP//B3LYP-D3BJ/def2-SVP, whereas 11.5 kcal/mol is obtained from SMD(THF)-MN15/def2-TZVP//B3LYP-D3BJ/def2-SVP. All Gibbs energy values in the text and figures are quoted in kcal/mol. All calculations were submitted and analyzed using the *CHEMSMART* package. Non-covalent interactions (NCIs) were analyzed using *NCIPLOT*[17] calculations combined with *CHEMSMART* commands. The .wfn files for *NCIPLOT* were generated at B3LYP-D3BJ/DGDZVP[18,19] level of theory. NCI indices calculated with *NCIPLOT* were visualized at a gradient isosurface value of s = 0.5 au. These are colored according to the sign of the second eigenvalue (λ_2) of the Laplacian of the density ($\nabla^2\rho$) over the range from −0.1 (blue = attractive) to +0.1 (red = repulsive). Optimized structures and molecular orbitals are prepared and visualized using *PyMOL* software[20], and the coresponding *PyMOL* session files (.pse) were generated using *CHEMSMART* commands.

Distortion/interaction (D/I)[21,22] analysis is applied to **TS1** and **TS1'** to discern the factors affecting *Z*/*E* selectivity. The transition state structures are decomposed by dividing the Fe–ligand–allene (fragment 1) and the ethyl radical (fragment 2) as two components. Single point calculations at SMD(THF) solvent correction were applied performed at both

B3LYP-D3BJ/def2-TZVP and MN15/def2-TZVP level of theory to obtain distortion and interaction energies. The distortion energy is given by:

$E_{dist} = E_{TS,frag1} + E_{TS,frag2} - (E_{eq,frag1} + E_{eq,frag2})$

where *TS,frag1,2* represent individual fragments in their distorted transition state geometries; and *eq,frag1,2* represent individual fragments in their optimized, equilibrium ground-state geometries; the interaction energy is given by:

$E_{int} = E_{TS} - (E_{TS,frag1} + E_{TS,frag2})$

which accounts for the stabilizing interactions (e.g., electrostatic, orbital, dispersion) between the distorted fragments in the TS.

Thus, the total activation energy is given by:

$\Delta E^{\ddagger} = E_{dist} + E_{int.}$

Note that this single-point activation energy and the activation energy difference $\Delta\Delta E^{\ddagger}$ between **TS1** and **TS1'** may be different from the Gibbs energy difference $\Delta\Delta G^{\ddagger}$.

II. Model reaction and DFT functional benchmarking

Scheme S1 shows the model reaction that we used for computational studies, corresponding to the product **14** in the experiment[23].

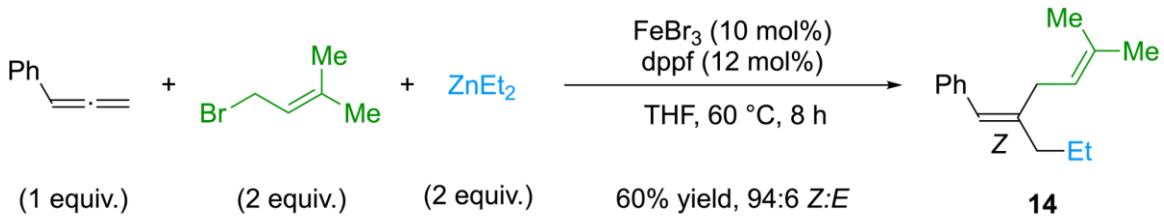

Scheme S1. Model reaction used for computational studies.

MN15 was selected as a complementary functional based on its reported performance for transition-metal energetics, spin-state ordering, and noncovalent interactions, as well as its application to related iron-catalyzed reactions.[12, 24–26]

To assess the functional dependence more broadly, we performed additional single-point calculations using hybrid meta-GGA TPSSh[27] (10% exact exchange) and local meta-GGA M06-L[28] (0%), alongside hybrid GGA B3LYP (20%) (with D3 dispersion correction and Becke–Johnson damping) and global-hybrid meta-NGA MN15 (44%). As summarized in Table S1, all four methods consistently predict the quintet state to be lowest in energy among the spin states examined for both **I** and **TS1**, despite quantitative differences in the spin-state energy gaps. For the other structures examined in multiple spin states, MN15 and B3LYP-D3BJ also give the same lowest-energy spin-state assignments.

Table S1. Relative Gibbs free energies of the singlet, triplet, and quintet states of **I** and **TS1** obtained using different single-point functionals with def2-TZVP basis set and SMD solvation model for THF. For each structure and functional, the corresponding quintet state is set to zero. All geometries were optimized at the B3LYP-D3BJ/def2-SVP level of theory and all energies are given in kcal/mol.

I		**B3LYP-D3BJ**	**MN15**	**TPSSh**	**M06-L**
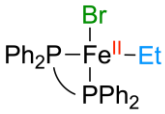	singlet	29.1	23.5	24.5	22.2
	triplet	11.7	3.0	8.6	10.7
	quintet	0.0	0.0	0.0	0.0
TS1		**B3LYP-D3BJ**	**MN15**	**TPSSh**	**M06-L**
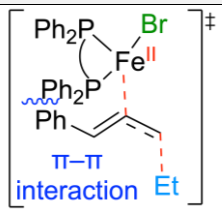	singlet	21.8	15.9	18.1	23.3
	triplet	3.5	22.6	1.8	4.7
	quintet	0.0	0.0	0.0	0.0

III. Formation and regeneration of species I

Based on our previous mechanistic proposal[24], the thermodynamic feasibility of both the initial formation and subsequent regeneration of the catalytically active Fe(II) species **I** was evaluated. As shown in Scheme S2, at the beginning of the reaction, the Fe(III) precatalyst undergoes ligand coordination, reduction, and transmetalation in the presence of dppf and $ZnEt_2$ to generate the bisphosphine-ligated Fe(II) alkyl bromide complex **I**. This overall process is accompanied by formation of $ZnBr_2$ and one-half equivalent of *n*-butane through coupling of two ethyl groups. The calculated reaction Gibbs energy is −51.2 (−55.8) kcal/mol, indicating that formation of **I** from the precatalyst is strongly thermodynamically favorable under the reaction conditions. At the end of the catalytic cycle, release of the dialkylated alkene product occurs together with regeneration of **I** and generation of the allylic radical required for the subsequent catalytic turnover. The corresponding overall reaction is also exergonic, with a calculated reaction Gibbs energy of −17.5 (−10.7) kcal/mol. These results indicate that both the initial generation and catalytic regeneration of **I** are thermodynamically feasible and are consistent with the proposed closed catalytic cycle.

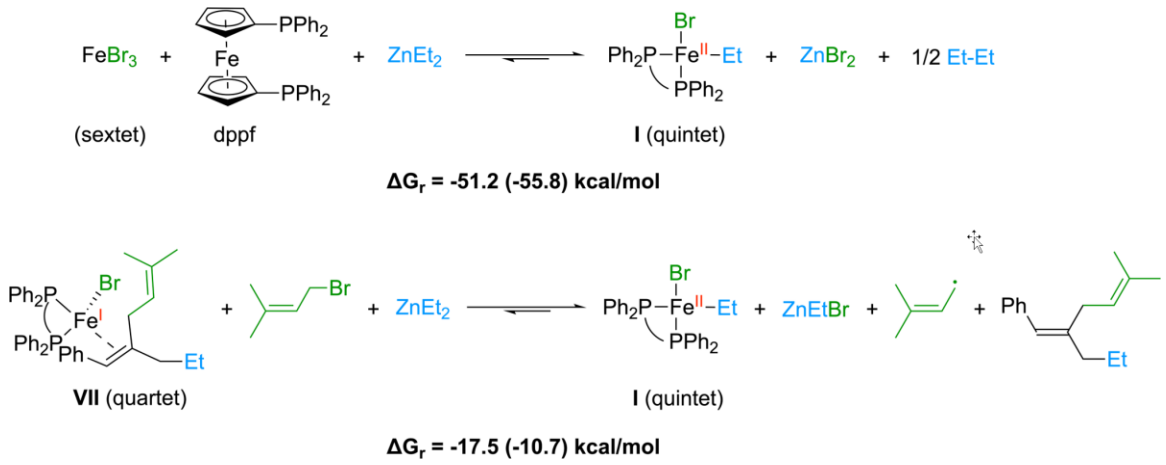

Scheme S2. Thermodynamic analysis of the formation and regeneration of the catalytically active Fe(II) species **I**. Calculated reaction Gibbs energies are given in kcal/mol, with MN15 single-point-corrected values shown in round brackets.

IV. Distortion/interaction analyses for TS1/TS1', TS3/TS3', and TS4/TS4'

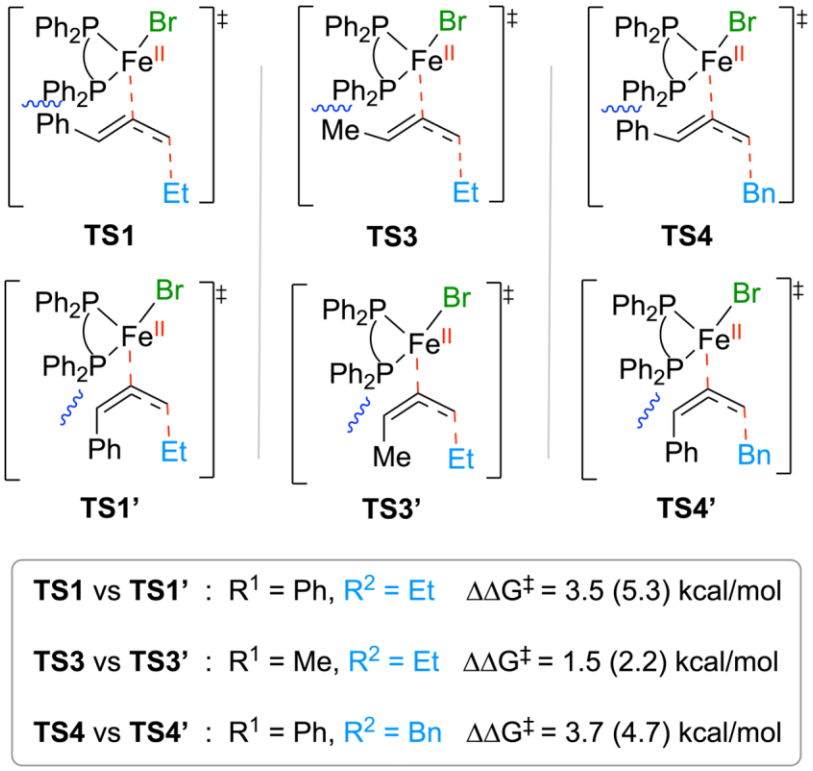

Figure S1. Competing radical-addition transition states with different allene and radical substituents. Energies are given in kcal/mol, with B3LYP-D3BJ values followed by MN15 values in parentheses.

The same fragmentation scheme used for **TS1**/**TS1'** was applied to **TS3**/**TS3'** and **TS4**/**TS4'** (Table S1). For the parent **TS1**/**TS1'** pair, the more favorable interfragment interaction in **TS1** compensates for the greater distortion penalty of the Fe–ligand–allene fragment. Replacing the allene phenyl substituent with methyl nearly eliminates this interaction-energy advantage: ΔE_{int} becomes 0.1 (0.1) kcal/mol for **TS3**/**TS3'**. Instead, **TS3** is favored primarily by the lower distortion energy of the Fe–ligand–allene fragment, with $\Delta E_{dist_1} = -1.3$ (−2.1) kcal/mol. For **TS4**/**TS4'**, the interfragment interaction favors **TS4** by 1.7 (2.7) kcal/mol. The lower distortion energy of the benzyl radical also favors **TS4** by 1.3 (1.3) kcal/mol, whereas the distortion-energy difference of the Fe–ligand–allene fragment is small. These contributions give an overall electronic-energy preference of 3.1

(4.1) kcal/mol for **TS4**. These results indicate that substituent changes alter the balance between distortion and interfragment interaction. Intrafragment contacts within the Fe–ligand–allene unit may influence this balance through their effects on its geometry and distortion energy.

Table S2. Distortion/interaction analysis of the competing transition-state pairs. Fragment 1 is the Fe–ligand–allene unit, and fragment 2 is the attacking ethyl or benzyl radical. Each energy difference is defined as the value for the unprimed transition state minus that for the corresponding primed transition state; negative values favor the unprimed structure (major product-forming transition state). Energies are given in kcal/mol, with MN15 values in parentheses.

	ΔE_{int}	ΔE_{dist_1}	ΔE_{dist_2}	$\Delta\Delta E^{\ddagger}$
TS1 vs **TS1'**	−2.9 (−4.0)	1.2 (1.8)	−0.2 (−0.2)	−1.9 (−2.5)
TS3 vs **TS3'**	0.1 (0.1)	−1.3 (−2.1)	−0.1 (−0.1)	−1.3 (−2.1)
TS4 vs **TS4'**	−1.7 (−2.7)	−0.1 (−0.1)	−1.3 (−1.3)	−3.1 (−4.1)

V. Visualization for DFT-optimized structures

	TS1	**TS1'**
$\Delta G^{\ddagger}$	26.4 (25.1)	29.9 (30.4)
DFT optimized structure	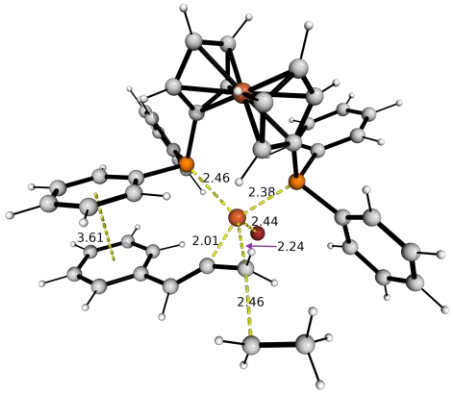	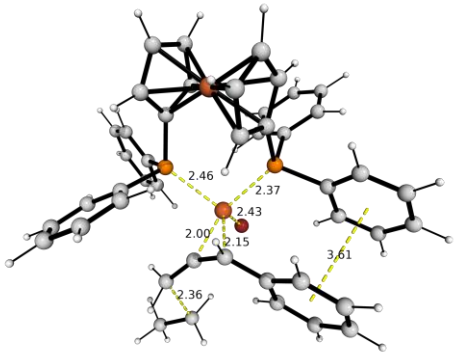

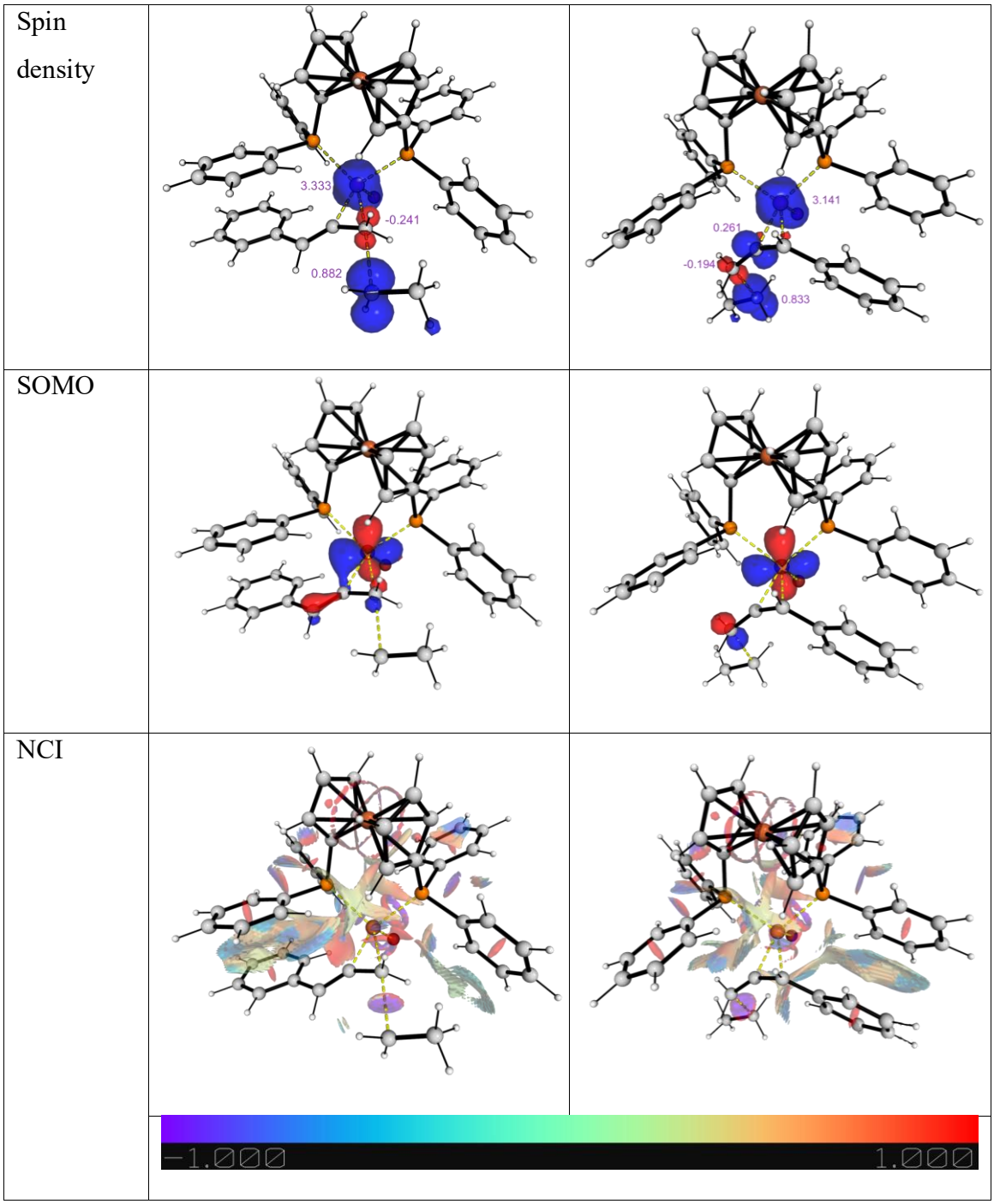

Figure S2. Detailed analysis of the competing transition states for the rate-determining step. Spin density, singly occupied molecular orbitals (SOMO) and non-covalent interaction (NCI) plots are shown. Spin density plots were visualized at an isosurface value of 0.01 a.u., SOMOs are visualized at 0.05 a.u., and the NCI plots were visualized at an isosurface value for the gradient at 0.5 a.u.

	TS1	**TS1'**
$\Delta G^{\ddagger}$	26.4 (25.1)	29.9 (30.4)
DFT optimized structure	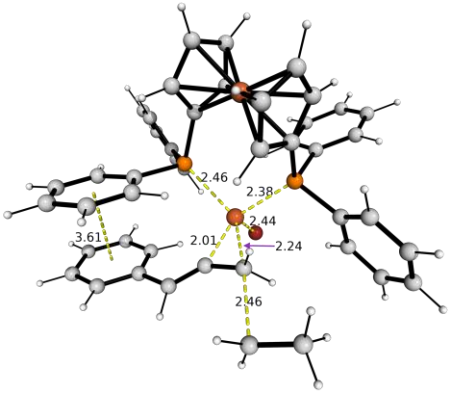	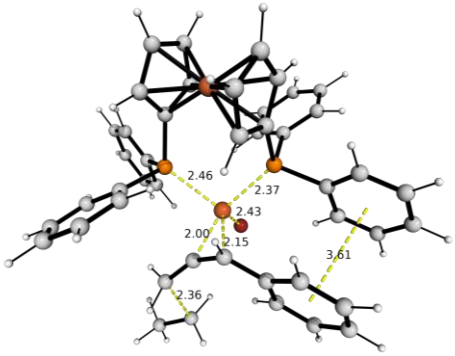
	TS1_c2	**TS1'_c2**
$\Delta G^{\ddagger}$	31.4 (32.4)	31.5 (31.2)
DFT optimized structure	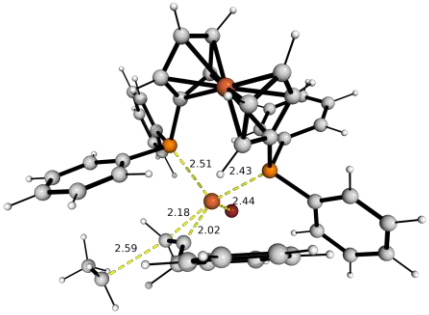	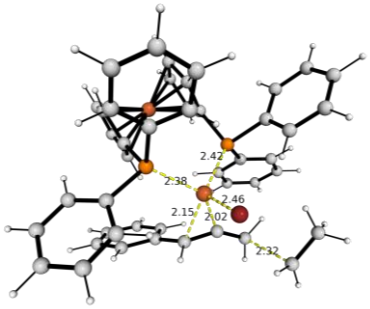
	TS1_c3	**TS1'_c3**
$\Delta G^{\ddagger}$	33.6 (35.2)	32.2 (32.3)
DFT optimized structure	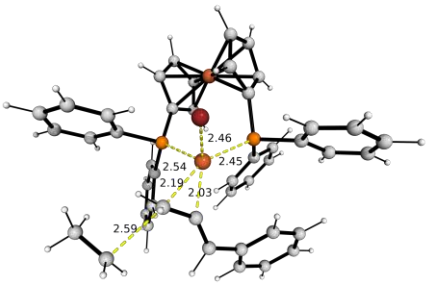	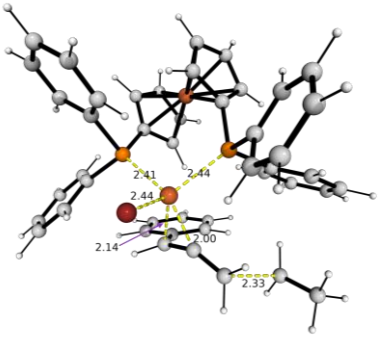

	TS1_c4	**TS1'_c4**
$\Delta G^{\ddagger}$	34.5 (53.2)	37.3 (40.8)
DFT optimized structure	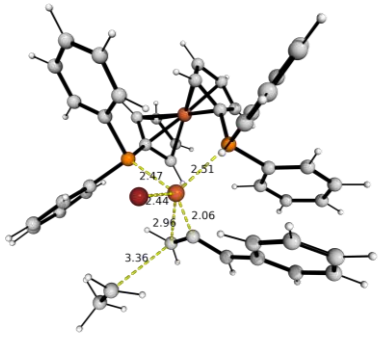	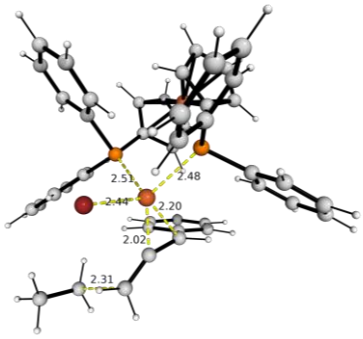
	TS1_triplet	**TS1'_triplet**
$\Delta G^{\ddagger}$	29.9 (47.7)	47.9 (50.5)
DFT optimized structure	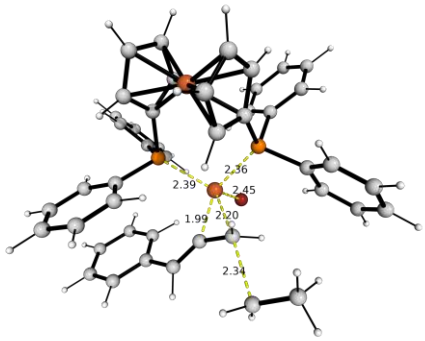	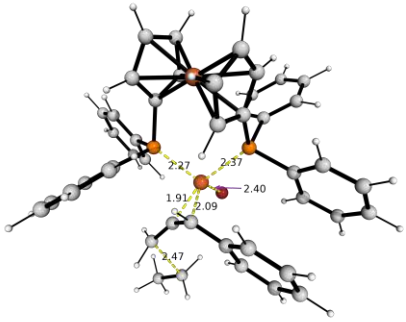
	TS1_singlet_os	**TS1'_singlet_os**
$\Delta G^{\ddagger}$	48.2 (41.0)	53.6 (47.0)
DFT optimized structure	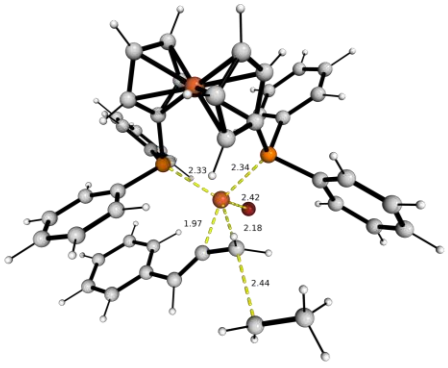	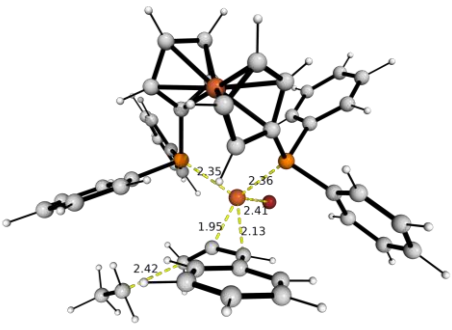

	TS1a	**TS1a'**
$\Delta G^{\ddagger}$	41.0 (38.3)	39.3 (35.9)
DFT optimized structure	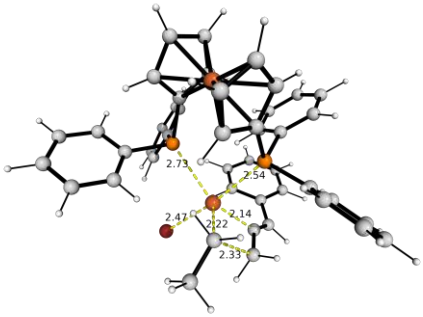	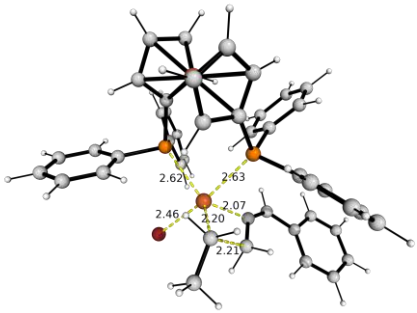
	TS1a_c2	**TS1a'_c2**
$\Delta G^{\ddagger}$	46.2 (42.0)	40.1 (38.0)
DFT optimized structure	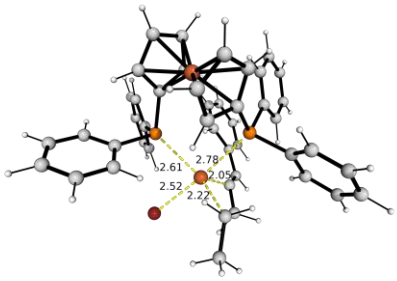	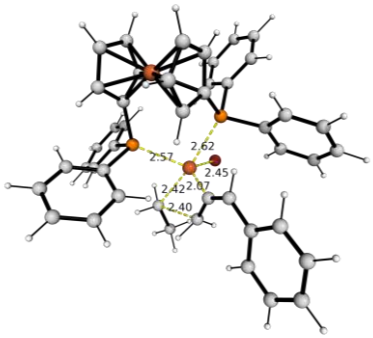
	TS2_quartet	**TS2_sextet**
$\Delta G^{\ddagger}$	−7.3 (−8.4)	−1.3 (−2.1)
DFT optimized structure	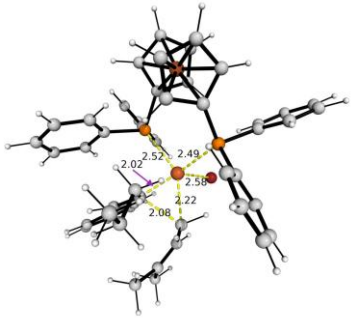	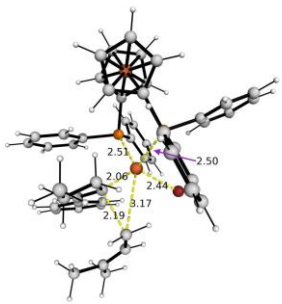
	TS1_L1	**TS1'_L1**

$\Delta\Delta G^{\ddagger}$	0.0 (0.0)	0.5 (−0.2)
DFT optimized structure	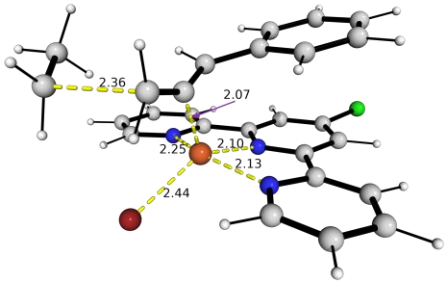	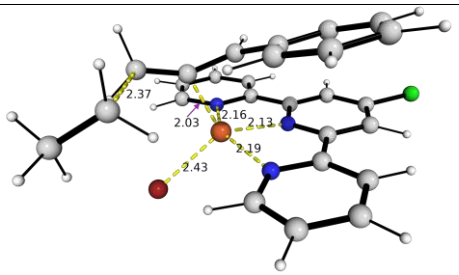
	TS1_allylic	**TS1_Fe_free**
$\Delta G^{\ddagger}$	41.7 (43.4)	30.8 (30.2)
DFT optimized structure	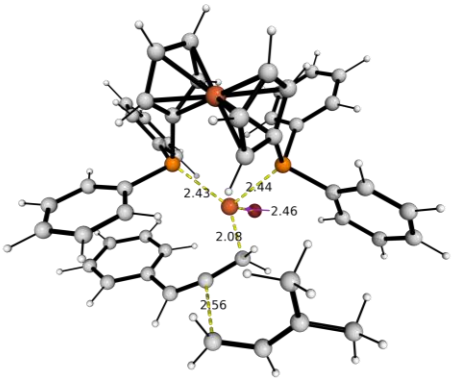	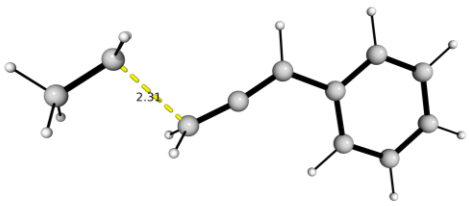
	TS3	**TS3'**
$\Delta\Delta G^{\ddagger}$	0.0 (0.0)	1.5 (2.2)
DFT optimized structure	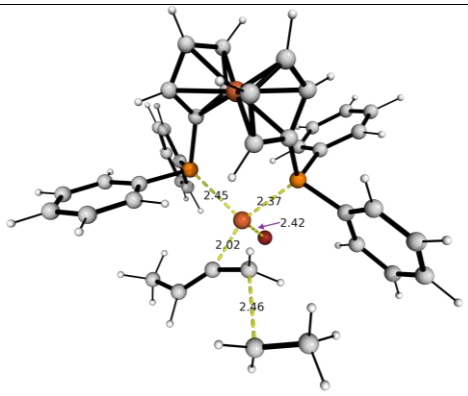	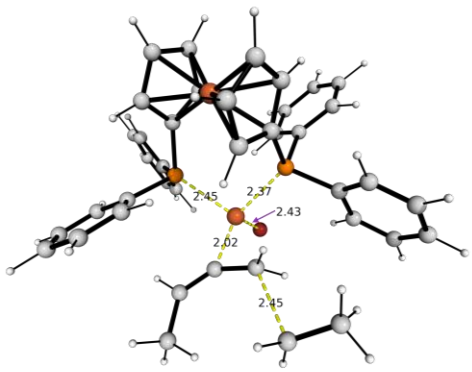
	TS4	**TS4'**
$\Delta\Delta G^{\ddagger}$	0.0 (0.0)	3.7 (4.7)

DFT optimized structure	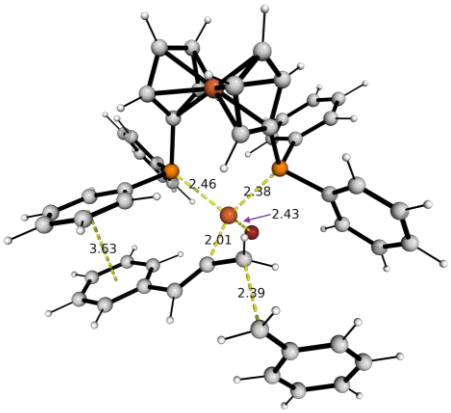	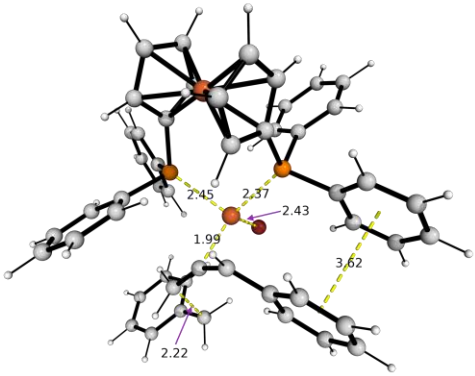
	TS5	**TS6**
$\Delta G^{\ddagger}$	39.4 (37.5)	34.0 (31.8)
DFT optimized structure	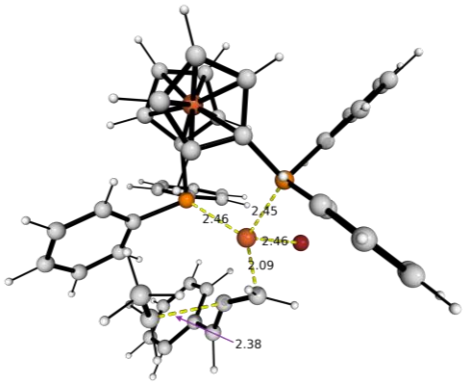	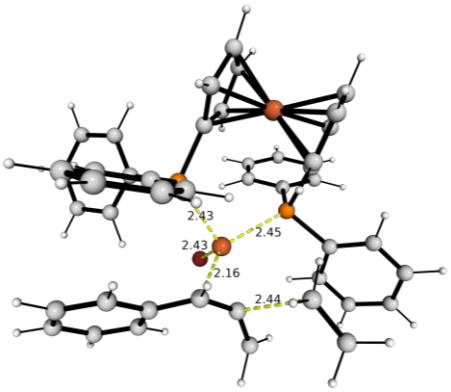

Figure S3. DFT optimized structures for transition states. The Gibbs free energies are given with **I_quintet** at the SMD(THF)-B3LYP-D3BJ/def2-TZVP//B3LYP-D3BJ/def2-SVP and SMD(THF)-MN15/def2-TZVP//B3LYP-D3BJ/def2-SVP level (in round brackets).

	I_singlet	**I_triplet**
Δ*G*	29.1 (23.5)	11.7 (3.0)
DFT optimized structure	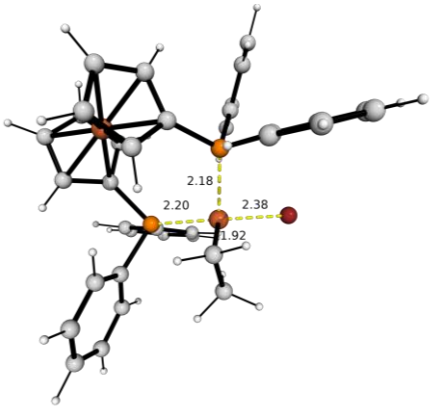	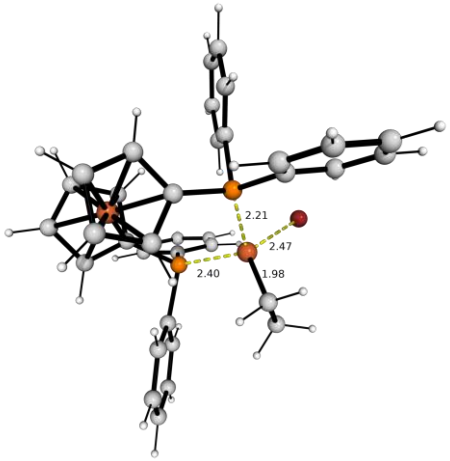
	I_quintet	**II_quintet**
Δ*G*	0.0 (0.0)	7.2 (6.1)
DFT optimized structure	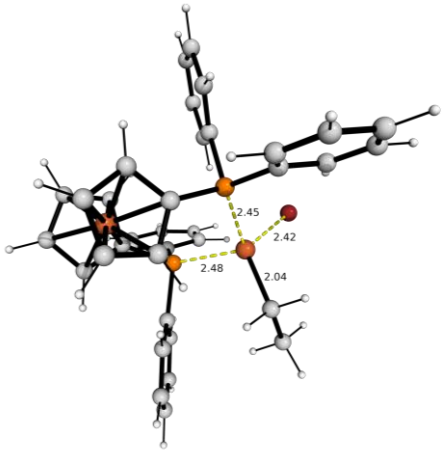	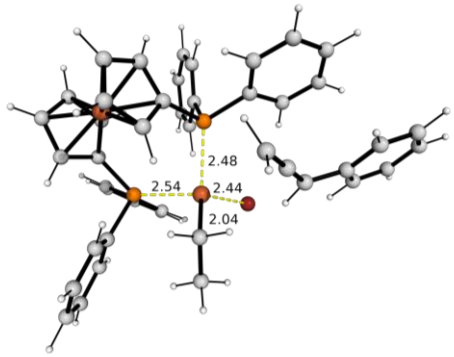
	III_quintet	**IV_quintet**
Δ*G*	20.5 (16.9)	−21.5 (−23.1)

DFT optimized structure	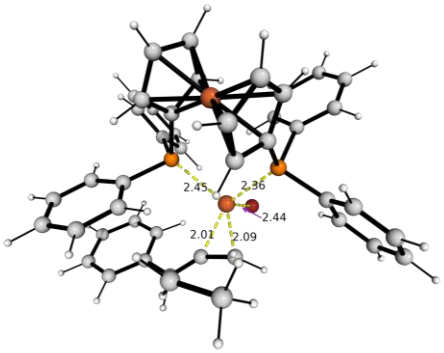	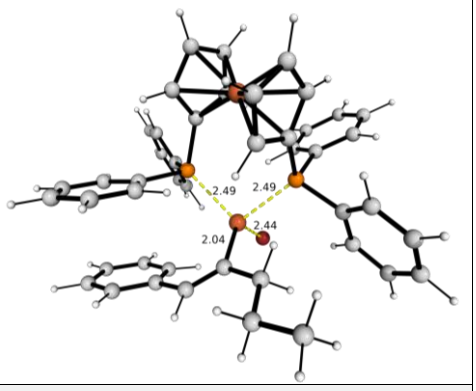
	IV'_quintet	**V_doublet**
Δ*G*	−18.2 (−18.1)	13.8 (15.4)
DFT optimized structure	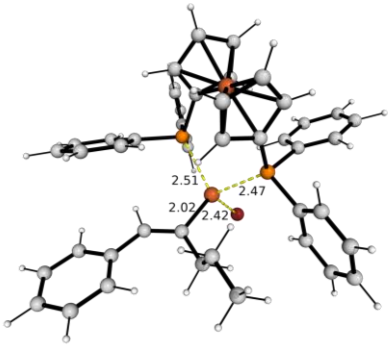	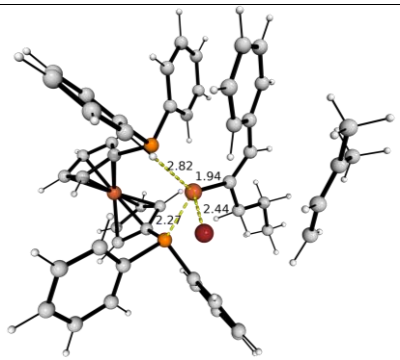
	V_quartet	**V_sextet**
Δ*G*	−14.6 (−1.0)	−15.1 (−18.5)
DFT optimized structure	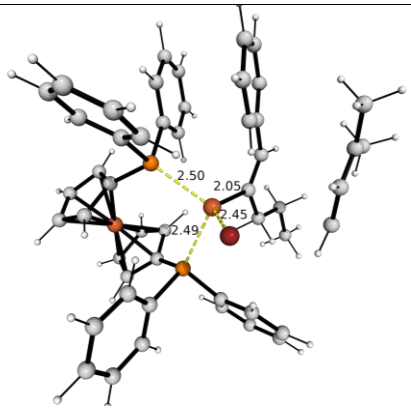	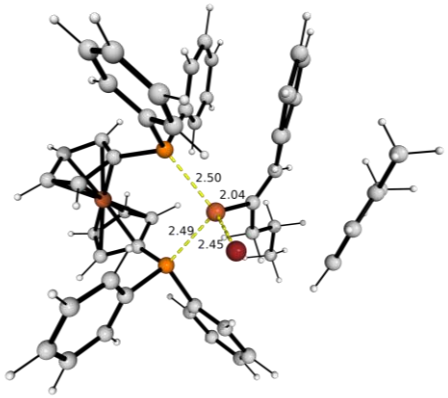
	VI_quartet	**VII_quartet**
Δ*G*	−12.2 (−14.4)	−41.9 (−52.3)

DFT optimized structure	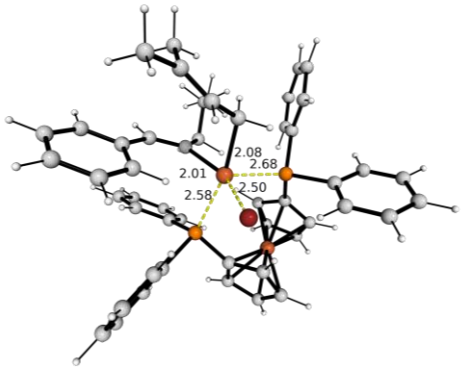	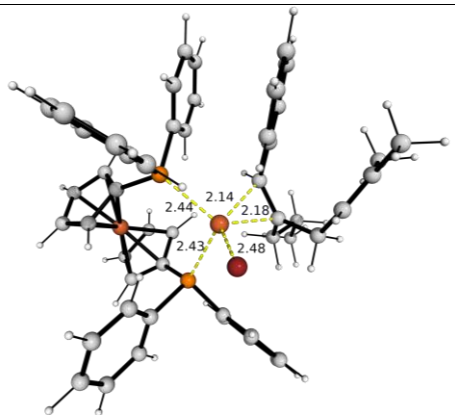
	VII_sextet	**III'_quintet**
Δ*G*	−14.7 (−18.1)	21.6 (19.7)
DFT optimized structure	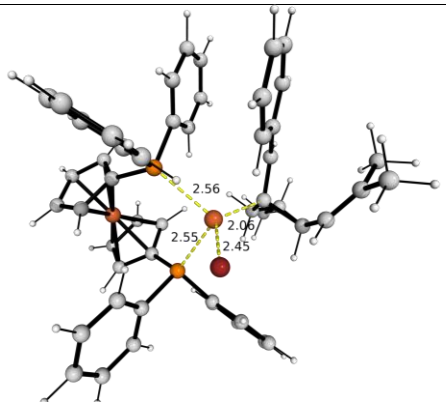	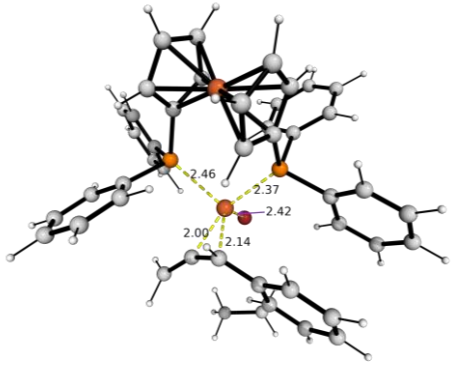
	Fe_I_complex_doublet	**Fe_I_complex_quartet**
ΔΔ*G*	26.0 (29.6)	0.0 (0.0)
DFT optimized structure	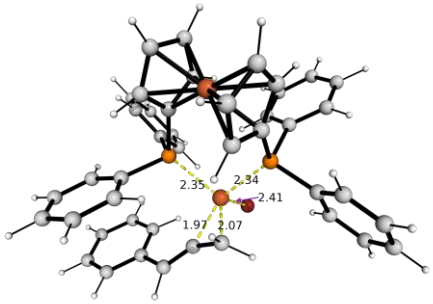	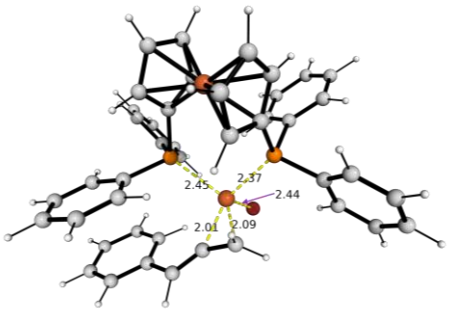
	***Z*_product**	***E*_product**

$\Delta\Delta G$	0.2 (0.04)	0.0 (0.0)
DFT optimized structure	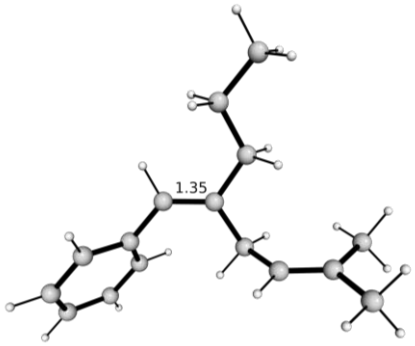	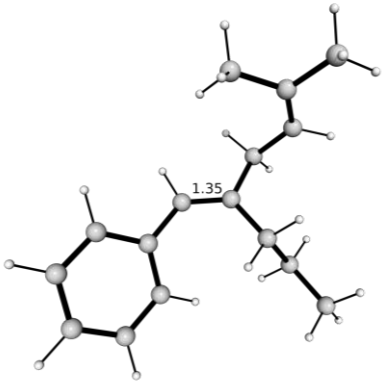

Figure S4. DFT optimized structures for intermediates and products. The Gibbs free energies are given with **I_quintet** at the SMD(THF)-B3LYP-D3BJ/def2-TZVP//B3LYP-D3BJ/def2-SVP and SMD(THF)-MN15/def2-TZVP//B3LYP-D3BJ/def2-SVP level (in round brackets).

VI. Optimized structures and absolute energies

Geometries of all optimized structures (in *.xyz* format with their associated energy in Hartrees) are included in a separate folder named *DFT_optimized_structures* with an associated readme.txt file. For the convenience of *.xyz* file management and usage, "_prime" is used to represent ('). All these data have been deposited and uploaded to zenodo.org (https://doi.org/10.5281/zenodo.23879209).

Absolute values (in Hartrees) for SCF energy, zero-point vibrational energy (ZPE), enthalpy and quasi-harmonic Gibbs free energy (at 333.15 K/60 °C) for optimized structures are given below. Single-point corrections in SMD (THF) using B3LYP-D3BJ/def2-TZVP and MN15/def2-TZVP levels of theory are also included.

Table S3.

Structure	E/au	ZPE/au	H/au	T.S/au	qh-G(T)/au	SP SMD(THF)-B3LYP-D3BJ/def2-TZVP	SP SMD(THF)-MN15/def2-TZVP
phenylallene	-347.500243	0.137391	-347.352339	0.044581	-347.396993	-347.887587	-347.4009634
ethyl_radical	-79.105489	0.058818	-79.040995	0.029808	-79.070895	-79.19780953	-79.06973496
allyl_radical	-195.775691	0.121734	-195.644746	0.04087	-195.685707	-195.997869	-195.7013672
I_singlet	-7172.61447	0.589042	-7171.978153	0.126442	-7172.103299	-7176.994847	-7175.292039
I_triplet	-7174.595684	0.584451	-7173.962901	0.13265	-7174.093113	-7177.013908	-7175.316084
I_quintet	-7174.610012	0.583483	-7173.977102	0.137516	-7174.111625	-7177.028444	-7175.316758
II_quintet	-7522.13079	0.722664	-7521.347216	0.163501	-7521.506765	-7524.926993	-7522.730372
III_quintet	-7522.109212	0.720064	-7521.327775	0.162645	-7521.487651	-7524.903296	-7522.710772
TS1	-7522.10083	0.72044	-7521.320192	0.159297	-7521.476843	-7524.896317	-7522.700146
TS1_c2	-7522.094575	0.720304	-7521.31388	0.159758	-7521.470988	-7524.887877	-7522.688015
TS1_c3	-7522.091256	0.720547	-7521.310284	0.161027	-7521.467721	-7524.884433	-7522.683499
TS1_c4	-7522.086476	0.717985	-7521.307337	0.162539	-7521.466901	-7524.879068	-7522.650887
TS1'	-7522.097457	0.720931	-7521.316546	0.160071	-7521.473194	-7524.891063	-7522.691959
TS1'_c2	-7522.099297	0.721805	-7521.31784	0.157538	-7521.472879	-7524.890644	-7522.692783
TS1'_c3	-7522.096416	0.722075	-7521.314823	0.156542	-7521.469121	-7524.890338	-7522.691846

TS1'_c4	-7522.090663	0.721943	-7521.308997	0.158292	-7521.464411	-7524.881245	-7522.677305
TS1_triplet	-7522.097215	0.721249	-7521.316145	0.157367	-7521.471085	-7524.892854	-7522.666153
TS1_singlet_os	-7522.069011	0.720923	-7521.288123	0.157233	-7521.442522	-7524.864135	-7522.677365
TS1'_triplet	-7522.072623	0.721713	-7521.291289	0.158088	-7521.446213	-7524.864476	-7522.661938
TS1'_singlet_os	-7522.066103	0.722285	-7521.28446	0.153966	-7521.436428	-7524.85861	-7522.670878
TS1a	-7522.08795	0.722878	-7521.306013	0.154748	-7521.45878	-7524.878251	-7522.684144
TS1a_c2	-7522.077468	0.723898	-7521.294754	0.155372	-7521.447455	-7524.870831	-7522.679122
TS1a'	-7522.084672	0.72312	-7521.30234	0.159806	-7521.457688	-7524.878686	-7522.685879
TS1a'_c2	-7522.084798	0.723322	-7521.302194	0.158951	-7521.457301	-7524.877948	-7522.682956
IV_quintet	-7522.192235	0.72821	-7521.405157	0.156184	-7521.558744	-7524.982215	-7522.786372
IV'_quintet	-7522.181356	0.728997	-7521.39343	0.158991	-7521.548279	-7524.976419	-7522.777957
V_sextet	-7717.986051	0.851509	-7717.065518	0.179878	-7717.241803	-7720.990534	-7718.501162
V_doublet	-7717.947591	0.853489	-7717.026277	0.172928	-7717.196857	-7720.951084	-7718.453635
V_quartet	-7717.986322	0.851656	-7717.065709	0.179086	-7717.241283	-7720.990561	-7718.474086
VI_quartet	-7717.992824	0.855264	-7717.070103	0.173	-7717.240708	-7720.993809	-7718.502513
TS2_quartet	-7717.984077	0.854885	-7717.062354	0.17205	-7717.231888	-7720.986052	-7718.493096
VII_quartet	-7718.044443	0.857594	-7717.119913	0.172249	-7717.289706	-7721.043758	-7718.565545
TS2_sextet	-7717.970167	0.852275	-7717.050488	0.173864	-7717.221842	-7720.972632	-7718.479183
VII_sextet	-7717.994939	0.855024	-7717.072445	0.175273	-7717.244415	-7720.996215	-7718.506845
***Z*_product**	-622.5558	0.335339	-622.198061	0.075055	-622.271712	-623.2452905	-622.3433286
***E*_product**	-622.557144	0.335672	-622.19922	0.073901	-622.27204	-623.246613	-622.3444057
TS1_L1	-5465.728795	0.420246	-5465.269912	0.112713	-5465.381161	-5467.657208	-5466.335926
TS1_L1'	-5465.726818	0.420797	-5465.267563	0.11125	-5465.377983	-5467.657657	-5466.337387
$FeBr_3$	-8985.342491	0.002598	-8985.331432	0.047283	-8985.378643	-8986.480395	-8987.451015
dppf	-3257.858455	0.517223	-3257.301176	0.114616	-3257.412664	-3259.695015	-3257.73705
prenyl_bromide	-2769.692966	0.126392	-2769.555997	0.046459	-2769.60233	-2770.235775	-2770.242177
n_butane	-158.357378	0.131317	-158.218107	0.036542	-158.25479	-158.537666	-158.2882
$ZnEt_2$	-1937.523281	0.127817	-1937.384355	0.048852	-1937.431965	-1937.982556	-1937.972871
ZnEtBr	-4432.292191	0.065131	-4432.218545	0.041933	-4432.260543	-4432.985749	-4433.403539
$ZnBr_2$	-6927.049095	0.001734	-6927.040845	0.035577	-6927.076483	-6927.963619	-6928.810325

III'_quintet	-7522.1051	0.719089	-7521.324	0.166441	-7521.4866	-7524.8985	-7522.7032
INT1	-543.2879	0.260519	-543.00664	0.07042	-543.07655	-543.89299	-543.11284
Fe_I_complex_doublet	-7442.9619	0.660105	-7442.2472	0.144857	-7442.3898	-7445.6578	-7443.5859
Fe_I_complex_quartet	-7442.9934	0.659551	-7442.2791	0.145628	-7442.4227	-7445.6979	-7443.6317
TS1_Fe_free	-426.60096	0.198995	-426.38664	0.05835	-426.44441	-427.07896	-426.46126
TS1_allylic	-7638.7497	0.781849	-7637.9034	0.169088	-7638.0692	-7641.6731	-7639.3037
TS3	-7330.4631	0.66627	-7329.74	0.153245	-7329.8902	-7333.0547	-7331.1176
TS3'	-7330.4605	0.666637	-7329.7371	0.153398	-7329.8874	-7333.0526	-7331.1143
TS4	-7713.7411	0.775312	-7712.9023	0.168042	-7713.0663	-7716.7435	-7714.2862
TS4'	-7713.7392	0.775968	-7712.9	0.167461	-7713.0634	-7716.7386	-7714.2797
TS5	-7522.0867	0.72234	-7521.3052	0.154996	-7521.4582	-7524.8801	-7522.6848
TS6	-7522.0943	0.721507	-7521.3131	0.156159	-7521.4673	-7524.8871	-7522.6924
INT2	-426.61141	0.197428	-426.39667	0.064447	-426.46008	-427.08918	-426.47554
TS7	-543.26038	0.261512	-542.97962	0.067872	-543.04657	-543.86669	-543.07926
TS8	-543.27022	0.26098	-542.98993	0.067276	-543.05657	-543.87534	-543.08924
TS9	-543.25788	0.260646	-542.97776	0.068117	-543.0451	-543.86334	-543.07553

Absolute single-point energies (in Hartree) calculated using SMD(THF)-TPSSh/def2-TZVP and SMD(THF)-M06-L/def2-TZVP. All geometries were optimized at the B3LYP-D3BJ/def2-SVP level of theory.

Table S4.

Structure	SP SMD(THF)-TPSSh/def2-TZVP	SP SMD(THF)-M06-L/def2-TZVP
I_singlet	-7176.787176	-7176.318233
I_triplet	-7176.803909	-7176.327843
I_quintet	-7176.813389	-7176.340789
TS1_singlet	-7524.62199951	-7524.085072
TS1_triplet	-7524.647646	-7524.114413
TS1_quintet	-7524.648354	-7524.119739

References

1. *Gaussian 16*, Revision B.01; Gaussian, Inc.: Wallingford, CT, USA, 2016.
2. Becke, A. D. *J. Chem. Phys.* **1993**, *98*, 5648–5652. doi:10.1063/1.464913
3. Lee, C.; Yang, W.; Parr, R. G. *Phys. Rev. B* **1988**, *37*, 785–789. doi:10.1103/PhysRevB.37.785
4. Vosko, S. H.; Wilk, L.; Nusair, M. *Can. J. Phys.* **1980**, *58*, 1200–1211. doi:10.1139/p80-159
5. Stephens, P. J.; Devlin, F. J.; Chabalowski, C. F.; Frisch, M. J. *J. Phys. Chem.* **1994**, *98*, 11623–11627. doi:10.1021/j100096a001
6. Grimme, S.; Antony, J.; Ehrlich, S.; Krieg, H. *J. Chem. Phys.* **2010**, *132*, 154104. doi:10.1063/1.3382344
7. Weigend, F.; Ahlrichs, R. *Phys. Chem. Chem. Phys.* **2005**, *7*, 3297–3305. doi:10.1039/b508541a
8. Weigend, F. *Phys. Chem. Chem. Phys.* **2006**, *8*, 1057–1065. doi:10.1039/B515623H
9. Fukui, K. *J. Phys. Chem.* **1970**, *74*, 4161–4163. doi:10.1021/j100717a029

10. Fukui, K. *Acc. Chem. Res.* **1981**, *14*, 363–368. doi:10.1021/ar00072a001

11. Marenich, A. V.; Cramer, C. J.; Truhlar, D. G. *J. Phys. Chem. B* **2009**, *113*, 6378–6396. doi:10.1021/jp810292n

12. Yu, H. S.; He, X.; Li, S. L.; Truhlar, D. G. *Chem. Sci.* **2016**, *7*, 5032–5051. doi:10.1039/C6SC00705H

13. Grimme, S. *Chem. Eur. J.* **2012**, *18*, 9955–9964. doi:10.1002/chem.201200497

14. Li, Y.-P.; Gomes, J.; Mallikarjun Sharada, S.; Bell, A. T.; Head-Gordon, M. *J. Phys. Chem. C* **2015**, *119*, 1840–1850. doi:10.1021/jp509921r

15. Zhang, X.; Tan, H.; Liu, J.; Li, Z.; Wang, L.; Chen, B. W. J. *arXiv* **2025**, 2508.20042. doi:10.48550/arXiv.2508.20042

16. Bryantsev, V. S.; Diallo, M. S.; Goddard III, W. A. *J. Phys. Chem. B* **2008**, *112*, 9709–9719. doi:10.1021/jp802665d

17. Contreras-García, J.; Johnson, E. R.; Keinan, S.; Chaudret, R.; Piquemal, J.-P.; Beratan, D. N.; Yang, W. *J. Chem. Theory Comput.* **2011**, *7*, 625–632. doi:10.1021/ct100641a

18. Sosa, C.; Andzelm, J.; Elkin, B. C.; Wimmer, E.; Dobbs, K. D.; Dixon, D. A. *J. Phys. Chem.* **1992**, *96*, 6630–6636. doi:10.1021/j100195a022

19. Godbout, N.; Salahub, D. R.; Andzelm, J.; Wimmer, E. *Can. J. Chem.* **1992**, *70*, 560–571. doi:10.1139/v92-079

20. Schrödinger, L. The PyMOL Molecular Graphics Development Component, Version 1.8; **2015**.

21. Ess, D. H.; Houk, K. N. *J. Am. Chem. Soc.* **2007**, *129*, 10646–10647. doi:10.1021/ja0734086

22. Bickelhaupt, F. M.; Houk, K. N. *Angew. Chem. Int. Ed.* **2017**, *56*, 10070–10086. doi:10.1002/anie.201701486

23. Tan, T.-D.; Tee, K. Z.; Luo, X.; Qian, P.-C.; Zhang, X.; Koh, M. J. *Nat. Synth.* **2025**, *4*, 116–123. doi:10.1038/s44160-024-00658-7

24. Tan. T.-D.; Serviano, J. M. I.; Luo, X.; Qian, P.-C.; Holland, P. L.; Zhang, X.; Koh, M. J. *Nat. Catal*. **2024**, *7*, 321–329. doi:10.1038/s41929-024-01113-8

25. Verma, P.; Varga, Z.; Klein, J. E. M. N.; Cramer, C. J.; Que, L., Jr.; Truhlar, D. G. *Phys. Chem. Chem. Phys.* **2017**, *19*, 13049–13069. doi:10.1039/c7cp01263b

26. Dandu, N. K.; Reed, J. A.; Odoh, S. O. *J. Phys. Chem. C* **2018**, *122*, 1024–1036. doi:10.1021/acs.jpcc.7b09284

27. Tao, J. M.; Perdew, J. P.; Staroverov, V. N.; Scuseria, G. E. *Phys. Rev. Lett.* **2003**, *91*, 146401. doi:10.1103/PhysRevLett.91.146401

28. Zhao, Y.; Truhlar, D. G. *J. Chem. Phys.* **2006**, *125*, 194101. doi:10.1063/1.2370993